*GEOPHYSICAL RESEARCH LETTERS*

Supporting Information for

# Can glacial sea-level drop-induced gas hydrate dissociation cause submarine landslides?

Jinlong Liu[1], Shubhangi Gupta[2,3], Jonny Rutqvist[4], Yikai Ma[5], Shuhong Wang[1,*], Kuiyuan Wan[1], Chaoyan Fan[1], and Wen Yan[1,6]

[1]Key Laboratory of Ocean and Marginal Sea Geology, South China Sea Institute of Oceanology, Innovation Academy of South China Sea Ecology and Environmental Engineering, Chinese Academy of Sciences, Guangzhou 510301, China

[2]GEOMAR Helmholtz Centre for Ocean Research Kiel, Kiel, Germany

[3]Department of Geosciences, University of Malta, Msida, Malta

[4]Lawrence Berkeley National Laboratory, Berkeley, CA, USA

[5]South China Sea Standards and Metrology Center of State Oceanic Administration, Guangzhou 510300, China

[6]University of Chinese Academy of Sciences, Beijing 100049, China

Corresponding author: Shuhong Wang (wshds@scsio.ac.cn)

## Contents of this file



## Additional Supporting Information (Files uploaded separately)

## Introduction

The Supporting Information for this manuscript includes a detailed description of the model (i.e., Text S1, Figure S1 and Table S1), an extended sensitivity analysis of the model (i.e., Text S2, Figure S2 and Figure S3), and a description of the gas venting in the vicinity of the BGHSZ-seafloor intersection (i.e., Text S3 and Figure S4). BGHSZ is the abbreviation for the base of the gas hydrate stability zone.

## Text S1. A complete description of the model details

Hydrate dissociation, fluid flow and thermal behavior in the gas hydrate system were simulated using the parallel version of TOUGH+HYDRATE code with the kinetic hydrate reaction model (Moridis, 2014). At the end of the calculation, the pore pressure was imported into the FLAC3D geomechanical simulator to compute deformation with the Mohr−Coulomb elastoplastic mechanical model.

### Model domain

The model system is a two-dimensional slice of a slope located in the upper shallow water area of Sites 973-3 (seafloor water depth of 1026 m) and 973-4 (seafloor water depth of 1666 m) (Figures 1a and 1i). The model geometry is shown in Figure 1i, and the $z$ coordinates indicate the meters below current sea level (mbsl). The upper 260 m of the model domain (i.e., including the entire initial GHSZ) had a horizontal discretization of dx = 25 m, a 2D slice thickness of dy = 1 m, and a vertical discretization of dz = 1 m. The area below the upper 260 m of the model was discretized into 8 elements in the vertical direction. The model has 99900 gridblocks in total with the addition of gridblocks at the top, bottom, left and right boundaries. The mesh discretization in the FLAC3D calculation was the same as that in the TOUGH+HYDRATE simulation.

### Initial condition

Initially, the model was at the prevailing hydrostatic pressure. Based on the measured seafloor temperatures in the northern South China Sea (Yang et al., 2018), the seafloor temperature ($T_s$) at different water depths was fitted to exponentially decrease with increasing seafloor water depth (Figure S1):

$$T_s = 2.4639 + 21.3605e^{-2.6d_s} \quad (1)$$

where $d_s$ is the seafloor water depth in km. The seafloor temperature at the start time for the simulation was estimated by the current seafloor temperature ($T_s$) minus the temperature difference between 0 ka and the start time for the simulation (e.g., 35 ka or 124 ka), as shown on the blue line in Figure 1h (Bates et al., 2014). Based on the measured geothermal gradients in this area (Song et al., 2001; Yuan et al., 2009), the initial geothermal gradient ($T_G$) was assumed to linearly increase with the increase in seafloor water depth (Figure S1):

$$T_G = 26.48 + 17.16d_s \quad (2)$$

The pore spaces contained 40% hydrates (Handwerger et al., 2017) and 60% pore water (volume fraction) within the initial GHSZ. The initial hydrate saturation might be somewhat high for a real-world situation. This setting helped to avoid underestimating the overpressure and thus the likelihood of hydrate dissociation causing submarine landslides, as (1) Handwerger et al. (2017) indicated that the initially high hydrate content can leave submarine slopes in a state poised for failure upon removal of a certain amount of hydrate, and (2) it can result in low permeabilities due to hydrate occupation (e.g., the permeability reduction factor $k_{rS}$ is approximately $2.96\times10^{-3}$ (Table S1) for hydrate saturation $S_h = 40\%$) for inhibiting the rapid dissipation of the overpressure beneath the BGHSZ and thus facilitating the overpressure buildup (Liu & Flemings, 2009). This finding was also supported by Nixon & Grozic (2007), who demonstrated that the likelihood of slope failure would increase with increasing initial hydrate content within the sediments. Outside the initial GHSZ, the pore space was fully saturated with pore water containing a mass fraction of dissolved methane of $3.5\times10^{-5}$ kg/kg (Garg et al., 2008; Heeschen et al., 2005). The initial dissolved mass fraction of NaCl in the pore water (i.e., the initial salinity) was 0.0307 kg/kg (Yang & Lei, 2016).

For the geomechanical calculation, the initial velocities were zero. The in situ stress was set at an equilibrium state under gravity.

### Boundary condition

The top, bottom, left and right boundaries were open to allow mass and heat transfer. For the top boundary at the seafloor, the pressure and temperature varied with time, representing a decrease in ocean level (i.e., a decrease in hydrostatic pressure) (red line in Figure 1h) and a change in seafloor temperature (blue line in Figure 1h) during glacial periods (Bates et al., 2014). At the bottom boundary, the temperature was fixed, and the changes in pressure were as time-variable as that at the top boundary of the seafloor to approximate an instant drop in hydrostatic pressure in response to the sea-level drop.

In terms of geomechanical boundary conditions, the top boundary at the seafloor was allowed to move freely, and the bottom, left and right boundaries were fixed for normal displacement. In addition, a vertical stress representing the weight of the overlying water column was applied on the free moving top boundary.

### Model parameters and assumptions

The supplementary model parameters and equations are listed in Table S1.

For the geomechanical properties, we assumed that certain mechanical properties (bulk modulus, shear modulus and cohesion) increase linearly from the value with hydrate saturation $S_h = 0$ to the value with $S_h = 1$ in Table S1 (Masui et al., 2005; Rutqvist & Moridis, 2009). The bulk and shear moduli determined by the linear models generally matched the laboratory bulk and shear modulus data over the range of hydrate contents in this study (Waite et al., 2009). In the main simulations, the cohesion linear model was used as follows (Wang et al., 2020):

$$C = 0.07 + 0.076S_h \text{ (MPa)} \tag{3}$$

Equation (3) leads to hydrate-bearing sediment cohesion that ranges from 0.07 to 0.1004 MPa for a hydrate saturation between 0 and 40%. The resulting cohesion of hydrate-bearing sediments was small compared to the values derived from other models or laboratory data (Liu et al., 2018; Rutqvist & Moridis, 2009; Waite et al., 2009). The small cohesion was used to avoid underestimating the potential plastic deformation and the occurrence or extent of the potential plastic deformation zone.

To investigate the effects of the cohesion model on our simulation results, we applied a greater cohesion model in additional simulations in the sensitivity analysis, and the equation was fitted by Waite et al. (2009) based on the experimental data from Masui et al. (2005) and Masui et al. (2006):

$$C = 0.28 + 2.0S_h \text{ (MPa)} \tag{4}$$

## Text S2. Extended Sensitivity Analysis of the Model

In this section, we describe the influences of a rapid sea-level drop, a steep slope and a great cohesion model of hydrate-bearing sediments on the occurrence and extent of the potential plastic deformation zone.

### The rate of sea-level drop

We investigated the effects of an increase in the sea-level drop rate from 8 to 411.4 m/kyr, and 411.4 m/kyr (from −30.83 m at 54.37 ka to −59.63 m at 54.30 ka) was selected because it was possibly the maximum sea-level drop rate during the Quaternary (Miller et al., 2020). While keeping the sea-level drop amplitude and the other conditions constant in the low-angle slope case (i.e., 2.34°), an increase in the sea-level drop rate (i.e., increased from 8 to 411.4 m/kyr) will lead to a slight reduction in the extent of the potential plastic deformation zone, i.e., the deepest part of the potential plastic deformation zone was approximately 75 m shallower in the $z$-direction or 1000 m shorter in the $x$-direction (Figure S2a and Figure 2h). When an increase in the sea-level drop rate (i.e., increased from 8 to 411.4 m/kyr) occurred on a high-angle slope (i.e., 10°) (Figures S2d and S2b), its effects were similar to those in the low-angle slope case (i.e., 2.34°) (Figure S2a and Figure 2h). The aforementioned effects can be explained as follows. When an increased sea-level drop rate (i.e., 411.4 m/kyr) and a constant sea-level drop amplitude of 138.7 m were used, the decreased time interval of sea-level drop (i.e., 0.337 kyr) might be too short for the hydrates that were beneath the theoretical BGHSZ to completely dissociate. If the sea level remained constant after it had fallen by 138.7 m, the hydrates that were beneath the deep part of the theoretical BGHSZ could continue to dissociate, and 3 kyr later, the modeled potential plastic deformation zone (Figure S2e) became almost the same as that in the slow sea-level drop case (Figure S2b).

### The slope angle

When the slope angle was increased from 2.34° to 10°, the modeled plastic deformation zone decreased, i.e., the length of its top boundary (i.e., near-seafloor boundary) decreased from 1657 to 442 m (Figure S2b and Figure 2h). The low-angle and high-angle slope case simulations resulted in almost the same minimum depths of the top boundary (i.e., near-seafloor boundary) (i.e., $z = -530$ or −523 mbsl) and almost the same maximum depths of the top boundary (i.e., near-seafloor boundary) (i.e., $z = -600$ mbsl) and of the bottom boundary (i.e., BGHSZ boundary) (i.e., $z = -975$ or −1050 mbsl) (Figure S2b and Figure 2h). The maximum depths of the bottom boundary (i.e., BGHSZ boundary) were also similar when expressed in meters below the seafloor (i.e., −202 or −223 mbsf) (Figure S2b and Figure 2h). This result suggested that the depths of the plastic deformation zone boundaries were nearly independent of the slope angle and mainly controlled by the initial sea-level position. The length of the top boundary (i.e., near-seafloor boundary) of the plastic deformation zone varied with slope length between the minimum and maximum depths of the top boundary (i.e., near-seafloor boundary) (almost a constant depth interval of 70 to 77 m) (Figure S2b and Figure 2h); thus, it varied with slope angle.

The calculated displacement and the volumetric and shear strains in the high-angle slope case (i.e., 10°) (Figures 3e-3h and Figure 4b) have similar trends to those in the low-angle slope case (i.e., 2.34°), although the magnitudes of the calculated displacements and strains in the high-angle slope case were somewhat greater than those in the low-angle slope case. In the high-angle slope case, there were stronger comparisons of $x$-direction displacement across the BGHSZ boundary of the plastic deformation zone where $x > 1885$ m (Figures 3e and 4b), indicating potentially more significant sliding. However, these strong comparisons of $x$-direction displacement across the BGHSZ boundary of the plastic deformation zone

disappeared where $x > 4000$ m, i.e., the *x*-direction displacement was approximately zero either above or beneath the BGHSZ boundary of the plastic deformation zone when $x > 4000$ m (Figure 3e), indicating the stability and support from the sediments in this area to prevent large-scale sliding along the BGHSZ boundary of the plastic deformation zone if it could occur.

### Cohesion model of hydrate-bearing sediment

When using a relatively great cohesion model (equation (4)) that could lead to a hydrate-bearing sediment cohesion ranging from 0.28 to 1.08 MPa for a hydrate saturation between 0 and 40%, the plastic deformation zone became very small and only at the very tip of the GHSZ (Figures S2f, S2g and S2h).

We also conducted additional simulations in which the initial hydrates occurred only within a layer of 50 meters thick just above the BGHSZ or the grids were strictly rectangular in the model domain discretization as in Reagan et al. (2011) to examine the robustness of our modeling results, while all other model parameters were kept identical. If the initial hydrates were only within a layer of 50 meters thick above the BGHSZ, the simulation results were generally the same as those with hydrates within the entire GHSZ in the initial time (Figures 2e-2h and 3a-3d). When the grids were strictly rectangular in the model domain discretization, the modeled values and distribution of the overpressure were also generally the same as those in the main simulations (Figure 2g). These additional simulations did not change the general trends of our modeling results in the main simulations.

## Text S3. The gas venting in the vicinity of the BGHSZ-seafloor intersection

Most of the free gas from dissociated hydrates migrated up along the BGHSZ during glacial periods, and was emitted into the overlying ocean in the vicinity of the shallow end of the modeled base of hydrate zone (Figure S4). In addition, free gas release occurred at the seafloor between the modeled base of hydrate zone (the purple line in Figure S4) and the theoretical BGHSZ (the orange line in Figure S4). This was because the contact with overlying hydrostatic ocean water would facilitate overpressure dissipation (Figure 2g) and a shift in the boundary of the hydrate stability zone, which would lead to gradual hydrate dissociation toward greater water depths in this area (i.e., the near-seafloor area between the modeled base of hydrate zone and the theoretical BGHSZ). The free gas saturation in this area was relatively small and was difficult to distinguish in Figure 2f.

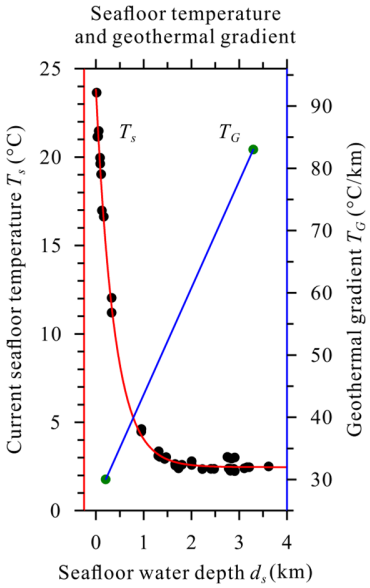


**Figure S1.** The black circles and fitted red line indicate the measured (Yang et al., 2018) and fitted current seafloor temperature ($T_s$) in the study area. The seafloor temperature at the simulation start time was estimated by $T_s$ minus the temperature difference between 0 ka and the simulation start time (e.g., 35 or 124 ka), as shown by the blue line in Figure 1h. The dark green circles and blue line indicate the measured (Song et al., 2001; Yuan et al., 2009) and fitted geothermal gradient, respectively, in the study area. The variable geothermal gradients were considered because geothermal gradients are not always constant along slopes due to sedimentation and distance from the locations of tectonic activity (Cloetingh et al., 2010). For example, a high geothermal gradient anomaly was suggested near a graben-bounding fault in the study area (Liao et al., 2014). The variation in the geothermal gradients used was slight (i.e., 34−40.5 °C/km) for the slope in Figure 1i.

(A) $\sigma_{v\_eff} - C$ (MPa) for $D_A$ = 138.7 m, $D_R$ = 411.4 m/kyr, $D_t$ = 0.337 kyr, $S_{an}$ = 2.34°, and $C$ = 0.076×$S_h$ + 0.07 (MPa)

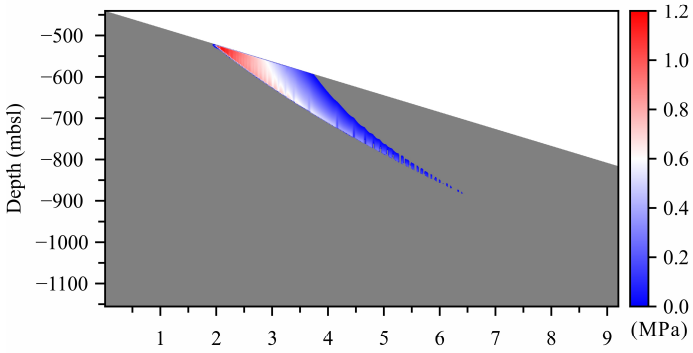


(B) $\sigma_{v\_eff} - C$ (MPa) for $D_A$ = 138.7 m, $D_R$ = 8.0 m/kyr, $D_t$ = 17.34 kyr, $S_{an}$ = 10.0°, and $C$ = 0.076×$S_h$ + 0.07 (MPa)

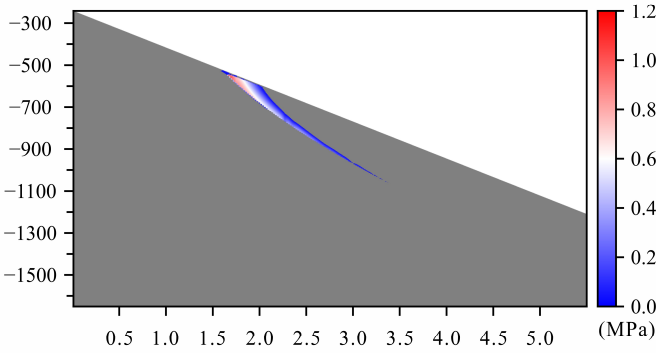


(C) $\sigma_{v\_eff} - C$ (MPa) for $D_A$ = 69.35 m, $D_R$ = 411.4 m/kyr, $D_t$ = 0.1686 kyr, $S_{an}$ = 10.0°, and $C$ = 0.076×$S_h$+0.07 (MPa)

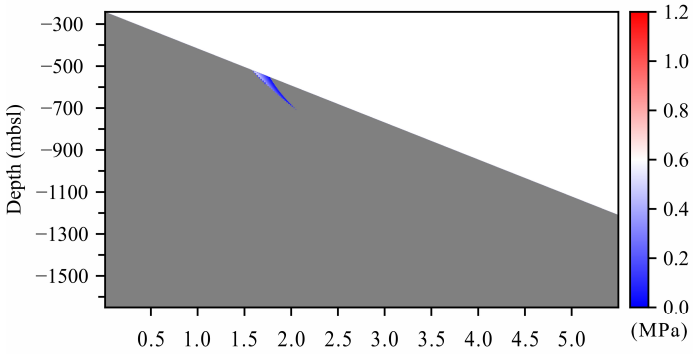


(D) $\sigma_{v\_eff} - C$ (MPa) for $D_A$ = 138.7 m, $D_R$ = 411.4 m/kyr, $D_t$ = 0.337 kyr, $S_{an}$ = 10.0°, and $C$ = 0.076×$S_h$+0.07 (MPa)

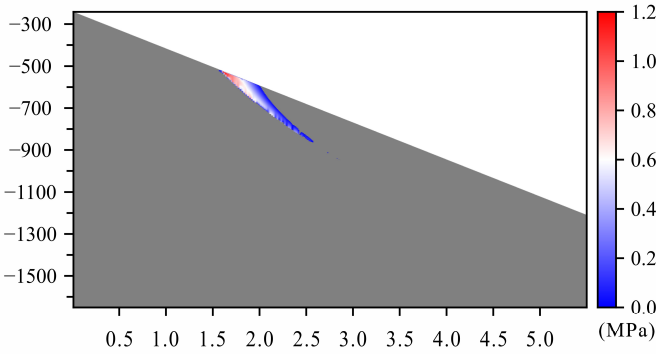


(E) $\sigma_{v\_eff} - C$ (MPa) at 3$^{th}$ kyr after the cessation of sea-level drops under $D_A$ = 138.7 m, $D_R$ = 411.4 m/kyr, $D_t$ = 0.337 kyr, $S_{an}$ = 10.0°, and $C$ = 0.076×$S_h$+0.07 (MPa)

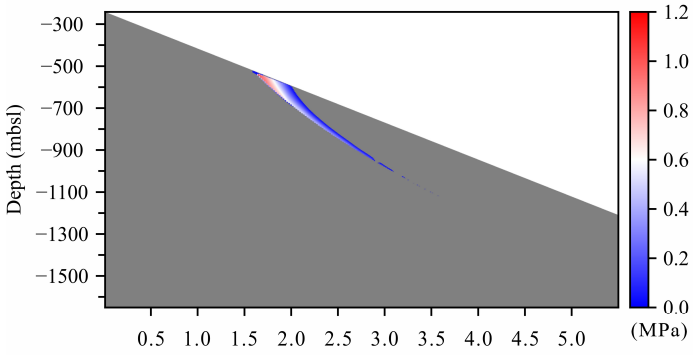


(F) $\sigma_{v\_eff} - C$ (MPa) for $D_A$ = 138.7 m, $D_R$ = 8.0 m/kyr, $D_t$ = 17.34 kyr, $S_{an}$ = 2.34°, and $C$ = 2.0×$S_h$+0.28 (MPa)

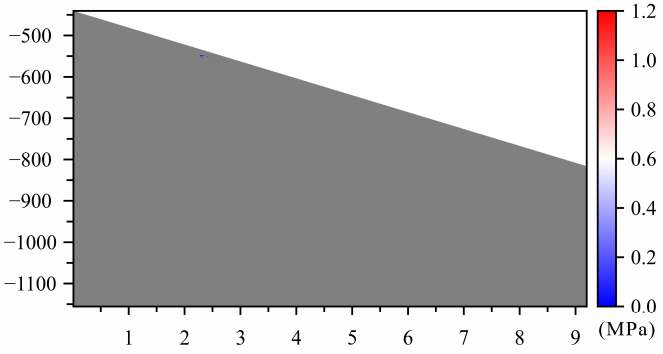


(G) $\sigma_{v\_eff} - C$ (MPa) for $D_A$ = 138.7 m, $D_R$ = 8.0 m/kyr, $D_t$ = 17.34 kyr, $S_{an}$ = 10.0°, and $C$ = 2.0×$S_h$+0.28 (MPa)

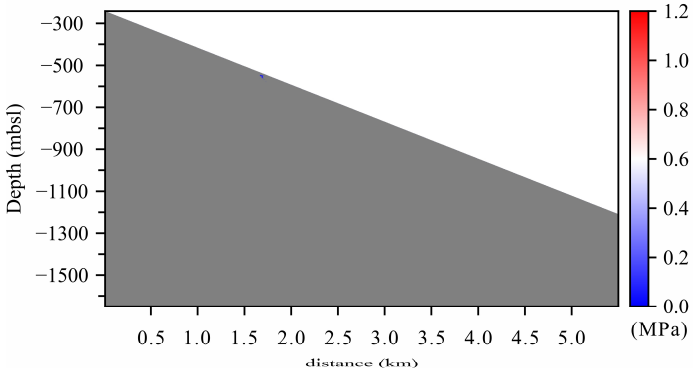


(H) $\sigma_{v\_eff} - C$ (MPa) for $D_A$ = 138.7 m, $D_R$ = 411.4 m/kyr, $D_t$ = 0.337 kyr, $S_{an}$ = 10.0°, and $C$ = 2.0×$S_h$+0.28 (MPa)

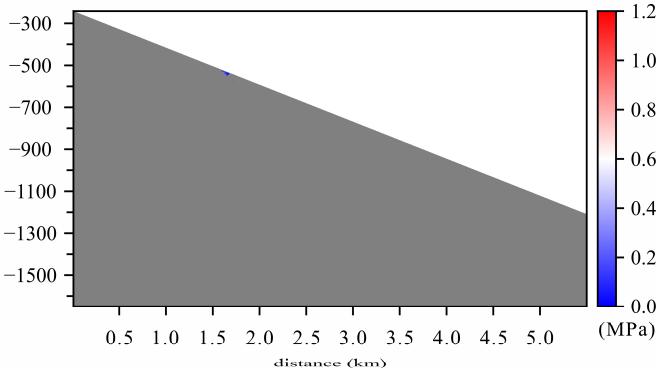

**Figure S2.** The vertical effective stress minus cohesion ( $\sigma_{v\_eff} - C$ ) (i.e., positive values for the potential plastic deformation zone) for several different simulation scenarios. $D_A$ , sea-level drop amplitude. $D_R$ , rate of sea-level drop. $D_t$ , time interval of sea-level drop. $S_{an}$ , slope angle. $S_h$ , hydrate saturation. In panels a-h, the gray areas represent $\sigma_{v\_eff} - C \leq 0$ .

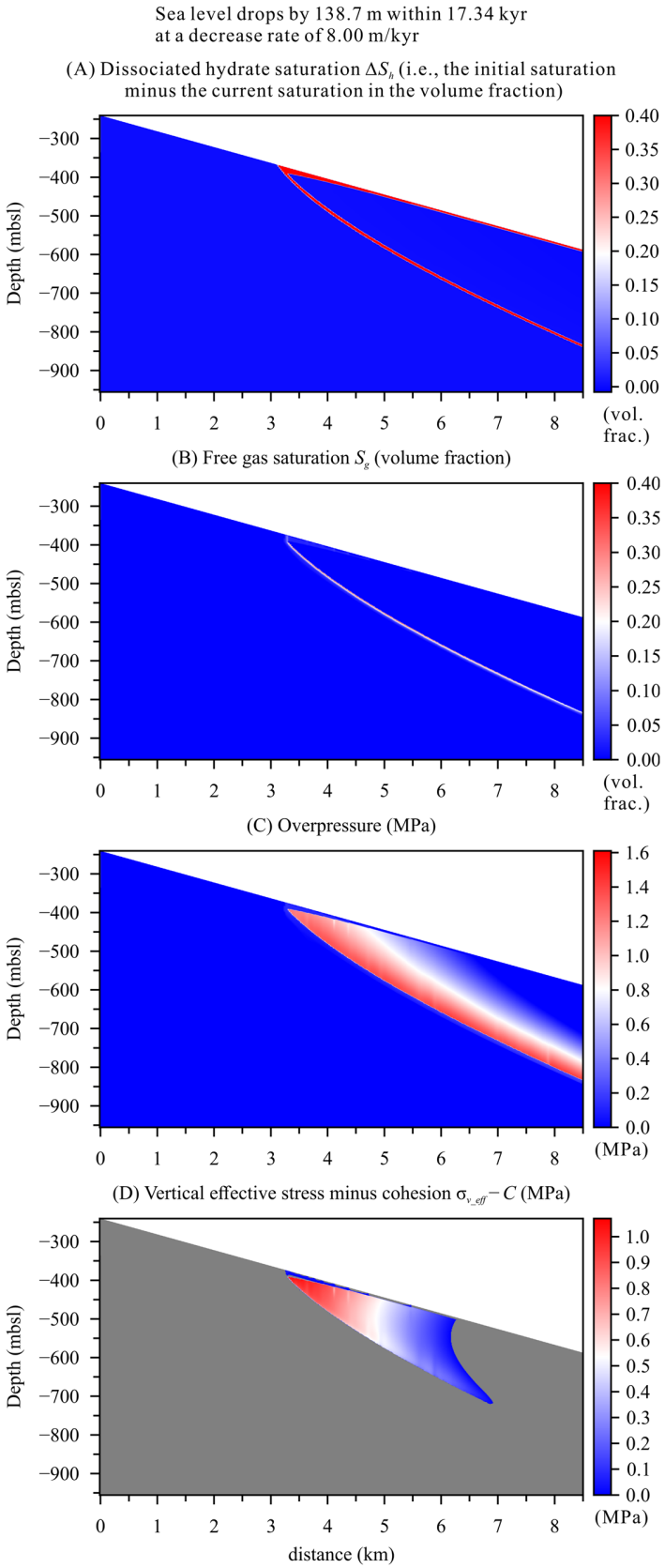
Sea level drops by 138.7 m within 17.34 kyr
at a decrease rate of 8.00 m/kyr
(A) Dissociated hydrate saturation ΔS_h (i.e., the initial saturation minus the current saturation in the volume fraction)
(B) Free gas saturation S_g (volume fraction)
(C) Overpressure (MPa)
(D) Vertical effective stress minus cohesion σ_v_eff − C (MPa)
Depth (mbsl)
−300
−400
−500
−600
−700
−800
−900
0
1
2
3
4
5
6
7
8
distance (km)
0.40
0.35
0.30
0.25
0.20
0.15
0.10
0.05
0.00
(vol. frac.)
1.6
1.4
1.2
1.0
0.8
0.6
0.4
0.2
0.0
(MPa)
1.0
0.9
0.8
0.7
0.6
0.5
0.4
0.3
0.2
0.1
0.0
(MPa)

**Figure S3.** Modeled (a) dissociated hydrate saturation (the initial hydrate saturation minus the current hydrate saturation in the volume fraction), (b) free gas saturation by volume fraction, (c) overpressure and (d) the vertical effective stress minus cohesion (positive values for the potential plastic deformation zone) in the simulation that resulted in the shallower BGHSZ-seafloor intersection and potential plastic deformation zone. In this simulation, the initial seafloor temperature and geothermal gradient were used as constant 3 °C (Berndt et al., 2014; Westbrook et al., 2009) and 30 °C/km (Reagan et al., 2011), respectively. The initial salinity was 0.035 kg/kg (Haacke et al., 2008; Westbrook et al., 2009). All other model parameters were kept identical to those in a main simulation in Figures 2e-2h in the manuscript. In this simulation, the modeled present-day BGHSZ-seafloor intersection was at approximately 370 mbsl, which was generally consistent with the water depth of 380–400 mbsl (Berndt et al., 2014; Reagan et al., 2011; Sarkar et al., 2012; Westbrook et al., 2009) at the BGHSZ-seafloor intersection off Svalbard.

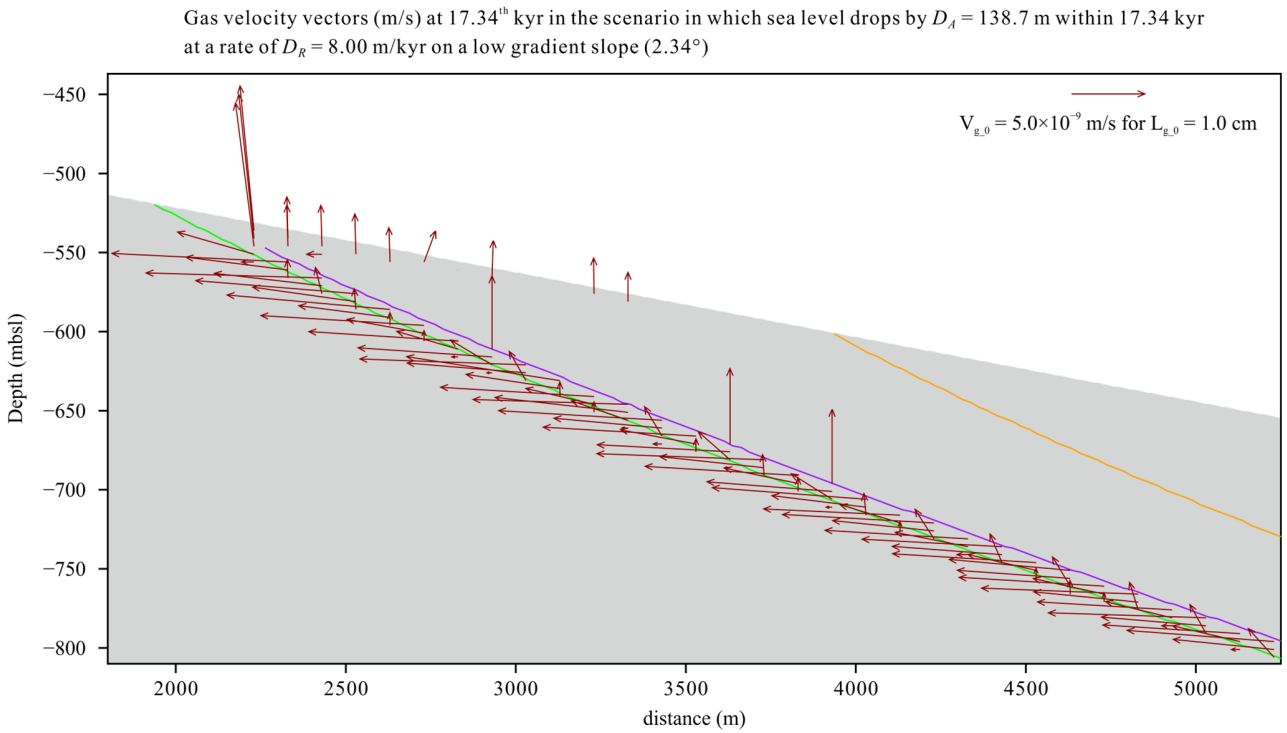


**Figure S4.** Modeled gas velocity vectors in the case of sea-level drops by 138.7 m at a rate of 8.0 m/kyr on a low gradient slope (2.34°). The magnitudes of the gas velocity vectors are $\left(\text{the lengths of gas velocity vectors}/L_{g\_0}\right)^5 \times V_{g\_0}$. The green, purple and orange lines in panels (a) and (b) indicate the locations of the initial BGHSZ, modeled base of hydrate zone after sea-level drops and theoretical BGHSZ after sea-level drops (assuming that the temperatures are the same as the initial temperatures and the pore pressure is hydrostatic), respectively.

| Parameter | Value | References |
|---|---|---|
| Sediment grain density | $2650\,\mathrm{kg/m^3}$ | (Garg et al., 2008) |
| Diffusivity of methane in brine ($D_m$) | $10^{-9}\,\mathrm{m^2/s}$ | (Garg et al., 2008) |
| Diffusivity of salt in brine ($D_s$) | $10^{-9}\,\mathrm{m^2/s}$ | (Garg et al., 2008) |
| Solid grain radius | $3.2848\times10^{-6}$ m | (Huang et al., 2022) |
| Pore compressibility ($\alpha_P$) | $10^{-8}$ $\mathrm{Pa^{-1}}$ | (Rutqvist & Moridis, 2009) |
| Porosity ($\phi_0$) as a function of depth ($d_{sf}$) below seafloor in mbsf | $\phi_0 = \phi_\infty + (\phi_1 - \phi_\infty)e^{-d_{sf}/B}$ | (Athy, 1930) |
| Minimum porosity at infinite depth ($\phi_\infty$) | 0.1 | (Daigle & Dugan, 2010) |
| Porosity at the seafloor ($\phi_1$) | 0.63 | (Daigle & Dugan, 2010) |
| The exponential decay constant (B) | 1400 m | (Daigle & Dugan, 2010) |
| Intrinsic permeability of sediments without hydrates ($k_0$) | $k_0 = e^{C_k\phi_0 + D}$ | (Neuzil, 1994) |
| Empirical coefficient ($C_k$) | 13 | (Daigle & Dugan, 2010) |
| Empirical coefficient ($D$) | –40 | (Daigle & Dugan, 2010) |
| Reduction factor on the intrinsic permeability due to hydrate presence (Modified Stone equation) | $k_{rS} = \left[\frac{\phi_0(1-S_h)-\phi_c}{\phi_0-\phi_c}\right]^{n_H}$ | (Moridis, 2014; Stone, 1970) |
| Critical porosity ($\phi_c$) | 0.01 | (Kossel et al., 2018) |
| Permeability reduction exponent due to hydrate occupation ($n_H$) | 11.4 | (Kossel et al., 2018) |
| Composite thermal conductivity model | $K_\Theta = (1-\phi_0)K_{dry} + \phi_0(S_aK_a + S_hK_h + S_gK_g)$ | (Gupta et al., 2015; Liu & Flemings, 2007; Smith et al., 2014) |
| Thermal conductivity of grains ($K_{dry}$) | 3.61 W $\mathrm{m^{-1}}$ $\mathrm{K^{-1}}$ | |
| Capillary pressure considering the presence of hydrate phase | $P_{cap} = \sqrt{\frac{1-S_h}{k_{rS}}}P_{cap,00}$ | (Moridis, 2014) |
| Capillary pressure for sediments free of hydrate phase (Van Genuchten-function) | $P_{cap,00} = -P_0\left[(S^*)^{-1/\lambda}-1\right]^{1-\lambda}$<br>$S^* = (S_a - S_{irA})/(S_{mxA} - S_{irA})$ | (Moridis, 2014; Van Genuchten, 1980) |
| Van Genuchten exponent ($\lambda$) | 0.87 | (Mahabadi et al., 2016) |
| Van-Genuchten's gas entry pressure ($P_0$) | $2.3\times10^5$ Pa | (Liu & Flemings, 2011) |
| Irreducible water saturation ($S_{irA}$) | 0.16 | (Mahabadi et al., 2016) |
| Maximum water saturation ($S_{mxA}$) | 1.0 | (Rutqvist & Moridis, 2009) |
| Maximum capillary pressure ($P_{cap,mx}$) | $6.5\times10^7$ Pa | (Liu & Flemings, 2011) |
| Relative permeability (Modified Stone's model) | $k_{rA} = \left[(S_a - S_{irA})/(1-S_{irA})\right]^n$<br>$k_{rG} = \left[(S_g - S_{irG})/(1-S_{irA})\right]^{n_G}$ | (Moridis, 2014) |
| Irreducible water saturation ($S_{irA}$) | 0.17 | (Mahabadi et al., 2016) |
| Irreducible gas saturation ($S_{irG}$) | 0.02 | (Mahabadi & Jang, 2014) |
| Relative permeability exponent ($n$) | 3.3 | (Mahabadi et al., 2016) |

| | | | |
|---|---|---|---|
| Relative permeability exponent ($n_G$) | | 3.1 | (Mahabadi et al., 2016) |
| Bulk Modulus ($K$) | $S_h = 0$ | 24 MPa | (Rutqvist & Moridis, 2009) |
| | $S_h = 1$ | 670 MPa | |
| Shear Modulus (G) | $S_h = 0$ | 22 MPa | (Rutqvist & Moridis, 2009) |
| | $S_h = 1$ | 612 MPa | |
| Cohesion ($C$) | $S_h = 0$ | 0.07 MPa | (Wang et al., 2020) |
| | $S_h = 1$ | 0.146 MPa | |
| Friction angle | | 37.2 | (Liu et al., 2018) |

**Table S1.** Model parameters and equations used in the main simulations.